JOURNAL OF COMPUTATIONAL PHYSICS 90, 431–457 (1990)

A Vlasov Code for the Numerical Simulation of Stimulated Raman Scattering

A. GHIZZO AND P. BERTRAND

Physique Théorique, Université de Nancy I, Nancy, France

M. M. SHOUCRI

Projet Tokamak, IREQ, Varennes, Québec, Canada

T. W. JOHNSTON

INRS-Énergie, Université du Québec, Varennes, Canada

E. FIJALKOW AND M. R. FEIX

PMMS/CNRS, Université d'Orléans, Orléans, France

Received April 10, 1988; revised September 21, 1989

Numerical simulations of the stimulated Raman scattering are presented using an Eulerian relativistic Vlasov code. Such a code allows a finer resolution in phase space than a particle code and provides a better understanding of the acceleration process for the particles at relativistically high energy. Forward Raman scattering as well as backward Raman scattering are considered to illustrate the possibilities of the Eulerian Vlasov code. © 1990 Academic Press, Inc.

INTRODUCTION

It is well known that an important obstacle to laser fusion is the production of high energy electrons. On the other hand, these relativistic electrons are of interest because of their application to laser-plasma accelerators, which have been proposed for the next generation of electron accelerators [1–2]. In this paper, we consider only electron acceleration by plasma waves generated through laser-plasma interaction and more precisely by stimulated Raman scattering (SRS). This scattering process has been isolated from other mechanisms of acceleration in several experiments showing the generation of fast electrons (see, for instance, Refs. [3–5]).

Numerical simulations have also been performed predicting the production of fast electrons by Raman scattering. These simulations involve P.I.C. codes [3, 5, 7] or the waterbag model [8]. Nevertheless, there is still the need to improve the understanding of the relativistic particle wave trapping and acceleration, of which the particle simulation gives only a very coarse description.

0021-9991/90 $3.00

On the other hand, the available vector computers point to the reactivation of the so-called Eulerian Vlasov codes [9–10] which afford a high phase space resolution. Recently, striking results have been obtained in the precise mechanism of nonlinear evolution of phase space holes associated with strong nonlinear plasma oscillations (two stream instability or Bernstein–Greene–Kruskal waves). These simulations are conducted over a long time (about $10^3\omega_p^{-1}$) performing the direct integration of the one-dimensional collisionless Vlasov–Poisson equations.

The central goal of the paper is to present a Vlasov code which affords the required resolution to discern the phase space dynamics of electrons accelerated by SRS. In Section 2, we present an extension of the one-dimensional Vlasov code to the electromagnetic relativistic case, providing a model suitable for describing Raman scattering. The simulation results are presented in Section 3 for the forward Raman scattering (FRS), while the backward Raman scattering (BRS) is discussed in Section 4.

2. The Eulerian Vlasov Code for SRS

2.1. *The Electrostatic Vlasov Code*

First, let us recall briefly the main features of a one-dimenional electrostatic Vlasov code. We want to solve the Vlasov equation for the one-dimensional electron (charge $-e$, mass m) plasma distribution function $f(x, p_x, t)$:

$$\frac{\partial f}{\partial t}+\frac{p_x}{m}\frac{\partial f}{\partial x}-eE_x\frac{\partial f}{\partial p_x}=0 \tag{1}$$

(where the longitudinal electric field E_x is given self-consistently by the Poisson equation), starting from a given initial condition $f(x, p_x, t=0)$. The best way is to separate the integration in both directions of the phase space plane [11–12]; this is the well-known splitting scheme. We have recently demonstrated [10] that this scheme is equivalent to solving the Vlasov equation (1) exactly, when the electric field $E_x(x, t)$ has been replaced by a succession of Dirac pulses E_x^*:

$$E_x^*(x, t)=E_x(x, t)\,\Delta T\sum_n \delta(t-t_{n+1/2}) \tag{2}$$

with $t_n=n\,\Delta T$, $t_{n+1/2}=(n+1/2)\,\Delta T$.

Denoting $t_{n+1/2}^-$ and $t_{n+1/2}^+$ as the time before and after the Dirac pulse, the integration during the time interval ΔT from t_n to t_{n+1} is straightforward and can be divided into three steps.

Step A1 ($t_n<t<t_{n+1/2}^-$). We have $E_x^*=0$ and

$$f(x, p_x, t_{n+1/2}^-)=f\left(x-\frac{p_x}{m}\frac{\Delta T}{2}, p_x, t_n\right). \tag{3}$$

Step A2 ($t = t_{n+1/2}$). Computing the electric field at time $t^-_{n+1/2}$ by substituting $f(x, p_x, t^-_{n+1/2})$ in the Poisson equation, we have

$$f(x, p_x, t^+_{n+1/2}) = f(x, p_x + e\,\Delta T\, E_x(x, t^-_{n+1/2}), t^-_{n+1/2}). \tag{4}$$

Note that $E^*_n(x, t^-_{n+1/2}) = E^*_n(x, t^+_{n+1/2})$, since Poisson's equation involves only $\int f\, dp_x$.

Step A3 ($t^+_{n+1/2} < t < t_{n+1}$). We repeat Step A1 starting from $f(x, p_x, t^+_{n+1/2})$ and obtaining $f(x, p_x, t_{n+1})$.

From a numerical point of view, this scheme is equivalent to integrating Eq. (1) along the characteristics and is correct to the second-order $(\Delta T)^2$ [11]. From a physical point of view, the fact that (3) and (4) give an exact solution of Eq. (1) with the replacement of E_x by E^*_x provides some interesting information on the size of ΔT, as already pointed out in [10]. For instance, linearizing (1) with E^*_x around an homogeneous equilibrium (i.e., $f(x, p_x, t) = n_0 F_0(p_x) + f_1(x, p_x, t)$) and performing the usual Laplace ($t \to s$)–Fourier ($x \to k$) transforms yields

$$-ik\left[E_x(k, s) + \frac{i\omega_p^2}{k}\sum_n E_x\left(k, s - \frac{2i\pi n}{\Delta T}\right)\int_{-\infty}^{+\infty} \frac{dF_0/dp_x}{s - ikp_x/m}\, dp_x\right]$$
$$= \int_{-\infty}^{+\infty} \frac{f_1(k, p_n, t=0)}{s - ikp_x/m}\, dp_x. \tag{5}$$

Due to the appearance of the sum $\sum_n$ on the l.h.s. of (5), the plasma dispersion function cannot be recovered. But, since we know that the frequency spectrum of the electric field does not exceed a few ω_p (plasma frequency), choosing ΔT such that $\omega_p\, \Delta T \ll 1$ results in a zero contribution for all terms of the sum on the l.h.s. of (5), except for $n = 0$, which recovers the usual Landau dispersion function.

Now, we have to consider the problem of effecting the shifts (3) or (4). Cubic spline interpolations have been used [13]. It can also be pointed out that during each time step, the Vlasov equation takes on the form of an advective equation (one over x, one over p_x) and antidiffusion methods can be used, leading to flux-corrected transport codes (FCT). Details on this numerical code have been given in Ref. [14]. On the other hand, the fact that a shift can be expressed in the corresponding Fourier space by simply changing the phase, suggests the use of the fast Fourier transform (FFT). This last code has been used to study the nonlinear behaviour of BGK waves [9, 10] and is found to be extremely stable over time of order $10^3 \omega_p^{-1}$.

The question, what is the best code, is still an open question. But detailed comparisons between the cubic spline code and the FFT code are now available [15]. Although both codes are extremely stable, up to $2{,}700\, \omega_p^{-1}$ and need about the same CPU time, better energy conservation and smaller storage memory requirements point to the use of the cubic spline code.

Finally, let us point out that every code requires a phase space discretization of the distribution function. Dividing the momentum space into N_p cells between $-P_{\max}$ and $+P_{\max}$(momentum cutoffs) and the length L of the plasma into N_x cells, requires $N_x N_p$ memory words. This memory requirement may be huge and is one of the main limitations of Eulerian Vlasov codes, especially if we want to extend it to $1\frac{1}{2}$D (one spatial dimension, 2 velocity dimensions) or 2D systems. For this reason, in the next paragraph, we will consider only a 1D Vlasov code.

2.2. *An Extension to the Relativistic Electromagnetic Case for SRS*

When an electromagnetic wave interacts with a plasma, the oscillatory electric field is perpendicular to the direction of propagation and produces only a quiver velocity. Charged particle acceleration can be achieved by a mechanism producing a longitudinal field. In Raman scattering, the ponderomotive force drives a large amplitude plasma wave along the laser wavevector direction and produces trapped electrons with very high momenta. To model this, we consider an infinite homogeneous plasma of density n_0, with a laser wavevector in the $+x$ direction: we specialize to wave propagation in one dimension, i.e., $\nabla = \hat{e}_x \partial/\partial x$, all field quantities being function of the space variable x only. Choosing the Coulomb gauge $\nabla \cdot \mathbf{A}$, the vector potential $\mathbf{A}$ is in the perpendicular (transverse) plan, i.e., $\mathbf{A} = \mathbf{A}_\perp$. Recalling that $\mathbf{E} = -\nabla\phi - \partial\mathbf{A}/\partial t$ we have

- in the transverse plane,

$$\mathbf{E}_\perp = -\partial\mathbf{A}/\partial t \tag{6}$$

- in the wave direction,

$$E_x = -\partial\phi/\partial x. \tag{7}$$

The electron distribution function $F(x, \mathbf{p}, t)$ obeys the relativistic Vlasov equation

$$\frac{\partial F}{\partial t} + \frac{p_x}{m\gamma}\frac{\partial F}{\partial x} - e(\mathbf{E} + \mathbf{u} \times \mathbf{B})\frac{\partial F}{\partial \mathbf{p}} = 0 \tag{8}$$

with the relativistic factor $\gamma = (1 + \mathbf{p}^2/m^2c^2)^{1/2}$.

As a matter of fact, the distribution function can be split into two parts:

- a nonrelativistic part depending on $\mathbf{p}_\perp$ and x,
- a relativistic part depending only on p_x and x.

The relativistic part occurs only for a small population of electrons which have been accelerated to high velocities by the trapping fields. For the nonrelativistic part, we have $\gamma \simeq 1$. Therefore we consider the following class of *exact* solutions of Eq. (8):

$$F(x, \mathbf{p}, t) = \delta(\mathbf{p}_\perp - e\mathbf{A})\, f(x, p_x, t), \tag{9}$$

where

$$f(x, p_x, t) = \int d\mathbf{p}_\perp F(x, \mathbf{p}, t) \text{ is the reduced distribution function,}$$

while $\mathbf{p}_\perp - e\mathbf{A}$ is the transverse canonical momentum. Note from Eq. (9) that the effective transverse motion of the particles is "cold." From the moments of F, and noticing that for the nonrelativistic part $\gamma \simeq 1$, we get the nonrelativistic version of the canonical transverse momentum conservation:

$$\mathbf{u}_\perp = e\mathbf{A}/m, \tag{10}$$

where $\mathbf{u}_\perp$ is the transverse fluid velocity.

For simplicity, the electric field $\mathbf{E}_\perp$ is in the y-direction ($\mathbf{E}_\perp = \hat{e}_y E_y$) and $\mathbf{B}$ in the z-direction ($\mathbf{B} = B_z \hat{e}_z$) (see Fig. 1). We have also $\mathbf{u}_\perp = u_y \hat{e}_y$. In the present geometry the function $f(x, p_x, t)$ defined in (9) satisfies the one-dimensional Vlasov equation:

$$\frac{\partial f}{\partial t} + \frac{p_x}{m\gamma}\frac{\partial f}{\partial x} - e(E_x + u_y B_z)\frac{\partial f}{\partial p_x} = 0. \tag{11}$$

Combining (10) and (6), u_y satisfies

$$\frac{\partial u_y}{\partial t} = -\frac{e}{m} E_y. \tag{12}$$

The electrostatic longitudinal self-consistent field E_x given by Eq. (7) obeys Poisson's equation with ions forming a fixed neutralizing background n_0:

$$\frac{\partial^2 \phi}{\partial x^2} = \frac{e}{\varepsilon_0}[n_e(x, t) - n_0], \tag{13}$$

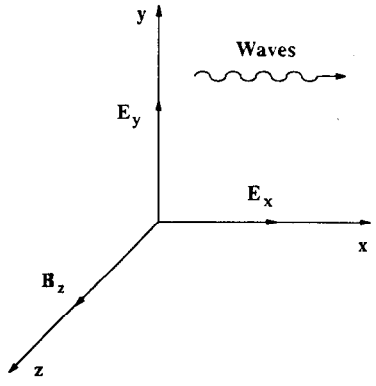

FIG. 1. Components of the electromagnetic fields.

where $n_e(x, t)$ is the electron density:

$$n_e(x, t) = \int_{-\infty}^{+\infty} f(x, p_x, t)\, dp_x. \tag{14}$$

The transverse electromagnetic field obeys Maxwell's equations,

$$\frac{\partial B_z}{\partial t} = -\frac{\partial E_y}{\partial x} \tag{15}$$

$$\frac{\partial E_y}{\partial t} = -c^2 \frac{\partial B_z}{\partial x} - \varepsilon_0^{-1} J_y, \tag{16}$$

where $J_y = -en_e(x, t)\, u_y(x, t)$ is the current density in the y-direction. For computational purposes, it is convenient to define

$$E^{\pm} = E_y \pm cB_z,$$

so that Eqs. (10) and (11) can be written

$$\left(\frac{\partial}{\partial t} \pm c \frac{\partial}{\partial x}\right) E^{\pm} = -\varepsilon_0^{-1} J_y, \tag{17}$$

which allows as to solve Maxwell's equation along their vacuum characteristics, $x \pm ct = \text{const}$ [16].

The way to solve the relativistic electromagnetic Vlasov equation is essentially the same as the electrostatic case and involves the three steps A1, A2, A3 described above. In Step A1 (or A3) we just have to introduce the relativistic factor, so that (3) must be replaced by

$$f(x, p_x, t^-_{n+1/2}) = f\left(x - \frac{p_x}{m\gamma} \frac{\Delta T}{2}, p_x, t_n\right).$$

In step A2, we have to add the ponderomotive force:

$$f(x, p_x, t^+_{n+1/2}) = f[x, p_x + e(E_x + u_y B_z)\, \Delta T, t^-_{n+1/2}].$$

This step requires the knowledge of the fields at $t^-_{n+1/2}$: the electrostatic field E_x not being affected by the shift A2 can be computed by solving Poisson's equation (13)–(14) at the end of step A1. But the necessary knowledge of the electromagnetic fields $E^{\pm}$ at time $t_{n+1/2}$ suggests solving Maxwell's equations (17) alternately with the Vlasov equation between $t_{n-1/2}$ to $t_{n+1/2}$ in a leapfrog scheme, in such a way that the contribution of the source terms in (11) and (17) are centered in time. Thus we again have three steps, denoting t_n^- and t_n^+ as the time before and after the application of the source terms—$\varepsilon_0^{-1} J_y$ considered as a Dirac pulse:

Step B1 ($t_{n-1/2} \leqslant t < t_n^-$). We solve (17) without source terms:

$$E^{\pm}(x, t_n^-) = E^{\pm}\left(x \mp c\frac{\Delta T}{2}, t_{n-1/2}\right). \tag{18}$$

Step B2 ($t = t_n$).

$$E^{\pm}(x, t_n^+) = E^{\pm}(x, t_n^-) - \Delta T\, \varepsilon_0^{-1} J_y(x, t_n^-).$$

Step B3 ($t_n^+ < t \leqslant t_{n+1/2}$). We repeat Step B1 and obtain the fields $E^{\pm}(x, t_{n+1/2})$ and consequently E_y and B_z at time $t_{n+1/2}$ so that Step A2 can be achieved (see Fig. 2).

Since c is a constant, the advective equation (18) could be solved by using grid spacing $\Delta x = c\,\Delta T/2$. But we want to be free of the choice of ΔT with respect to Δx, so that Fourier interpolation has been used in the present code.

Finally, Eq. (12) is solved between t_n and t_{n+1} using the time centered scheme

$$u_y(x, t_{n+1}) = u_y(x, t_n) - \frac{e}{m}\Delta T \frac{E^+(x, t_{n+1/2}) + E^-(x, t_{n+1/2})}{2}.$$

This code is equivalent to integrating the distribution function along the characteristics and is correct to the second order in ΔT (see Appendix).

In our numerical experiments, we use normalized quantities: t, x, u_y, p_x are normalized respectively to ω_p^{-1}, $l_0 = c/\omega_p$, c and $p_0 = mc$, where ω_p in the plasma angular frequency. The fields E_x or E_y are normalized to $\omega_p p_0/e$ and the density to n_0. The wave vectors k are normalized to ω_p/c.

Periodic boundary conditions are assumed. Although these conditions are somewhat far from real plasmas, they are used to exhibit the adequacy of our code in modelling SRS behaviour. The avantage of a periodic plasma as a test problem is that a rather small number of modes are needed. The simulations presented here are performed with a phase space grid of size $N_x N_p$ with typical values $N_x = 64$ and $N_p = 512$ or 1024. The time step is of order 0.03–0.06 ω_p^{-1}. Using a grid of 64×1024 or 65,636 entities = ("particles"), the CPU time is less than 2 μS per time step per entity ("particle") on a CRAY-2 computer. This code is optimized to make full use of vector facilities of CRAY-1-S or CRAY-2 computers.

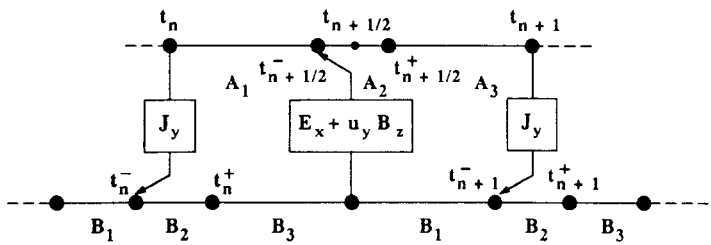

FIG. 2. Time stepping of Vlasov and Maxwell schemes.

3. The Forward Raman Scattering Problem (FRS)

The SRS instability is a parametric instability involving three waves: the incident electromagnetic wave, here referred to as the "pump" wave (ω_0, k_0) which drives two unstable waves; a scattered electromagnetic wave (ω_s, k_s); and an electron plasma wave (ω_e, k_e). The Raman instability occurs when the usual matching conditions hold,

$$\omega_0 = \omega_s + \omega_e \tag{19a}$$

$$k_0 = k_s + k_e, \tag{19b}$$

with the dispersion relation for the electron plasma wave given by the Bohm–Gross frequency $\omega^2 = \omega_p^2 + 3k^2 v_{\text{th}}^2$ and that for the two electromagnetic waves by $\omega^2 = \omega_p^2 + k^2 c^2$. The matching conditions (19) can be satisfied only if $n_e < n_{\text{crit}}/4$ when n_{crit} is the critical density above which electromagnetic radiation will not propagate. SRS instability is discussed in some detail in Ref. [17].

Due to the periodic character, we can select the different wavenumbers to obtain either forward scattering (FRS) with $\omega_s/k_s > 0$ or backward scattering $(\omega_s/k_s < 0)$ or any combination we want to study.

Let us first consider one case leading to FRS.

3.1. *Initial Condition*

We start with an initial homogeneous Maxwellian distribution with a thermal velocity $v_{\text{th}}/c = 0.17$ corresponding to a temperature $T_1 = 15$ keV, with a small fraction (α) of relativistic particles with $T_2 = 100$ keV (see experiments described in Ref. [5]),

$$F_0(p_x) = (1-\alpha)(2\pi m T_1)^{-1/2} \exp\left(-\frac{p_x^2}{2mT_1}\right) + \alpha C \exp\left(\frac{-mc^2(\gamma-1)}{T_2}\right)$$

with $\alpha = 0.05$, C is a normalization constant so that $\int F_0 \, dp_x = 1$. γ is the Lorentz factor. The cutoff in the momentum space is $\pm p_{\max} = \pm 6.5 \; mc$. The plasma is embedded in a periodic box of length $L = 10.47 \; c/\omega_p$ (or 61.1 λ_d, where $\lambda_d = v_{\text{th}}/\omega_p$ is the Debye length).

From now on, all quantities will be presented in the normalized units defined in 2.2. The initial (pump) electromagnetic wave is taken as

$$E_y = E_0 \cos k_0 x$$

$$B_z = \frac{k_0 E_0}{\omega_0} \cos k_0 x.$$

We recall that k_0 is normalized to ω_p/c, ω_0 to ω_p, and E_0 to $\omega_p mc/e$; choosing $k_0 = 2.4$ and $E_0 = 0.32$ we obtain

$$\omega_0 = (1 + k_0^2)^{12} = 2.6.$$

The quiver velocity (normalized to c) is

$$v_{\text{osc}} = E_0/\omega_0 = 0.123.$$

(For a 10.6 μm Co_2-laser the corresponding intensity in 1.8×10^{14} W/cm^2). The density as compared to the critical density is

$$n_0/n_{\text{crit}} = \omega_0^{-2} = 0.15.$$

With this choice, the prediction for FRS is 1.53 for the downshifted (Stokes) scattered frequency (with a wave number 1.16) and a Bohm–Gross frequency 1.07 (with a wave number 1.24).

It must be pointed out that a periodic code can handle only discrete wavenumbers which must be multiple of a fundamental mode $2\pi/L = 0.6$ (since $L = 10.47$, see above); thus, the electron distribution function is given a small initial perturbation on the mode k_e:

$$k_e = 2(2\pi/L) = 1.2, \qquad \text{coresponding to} \quad \omega_e = (1 + 3k_e^2 v_{\text{th}}^2)^{1/2} = 1.061.$$

These values are very close to the Bohm–Gross parameters mentioned just above. Consequently, we forcast the appearance of the Raman instability with the scattered mode

$$k_s = k_0 - k_e = 1.2 \qquad \text{corresponding to} \quad \omega_s = (1 + k_s^2)^{1/2} = 1.562.$$

For these selected wavenumbers, the mismatch from (19a), $\Delta\omega = \omega_s - (\omega_0 - \omega_e) = 0.024$, is sufficiently small. The total energy is 0.071. The relative variation of this quantity over the entire run (up to $825\omega_p^{-1}$) is less than 2.10^{-3}. The density conservation (i.e., $\int f\,dx\,dp_x$) is better than 10^{-8}.

3.2. *Energy Evolution and Manley Rowe Partition*

Figures 3a, b, c, d, show the different energies (in mc^2 units) as a function of time: the pump electromagnetic energy (mode k_0) the electromagnetic scattered energy (mode k_s), the electrostatic plasma energy (mode k_e) and the plasma kinetic energy defined as:

$$W_e = \frac{1}{L}\int_0^L \int_{-\infty}^{+\infty} (\gamma - 1) f(x, p_x)\,dx\,dp_x.$$

The electromagnetic energy is defined as

$$W_0 \quad (\text{or } W_s) = \frac{1}{L}\int_0^L \left(\frac{B_z^2}{2} + \frac{E_y^2}{2} + \frac{n_e u_y^2}{2}\right) dx,$$

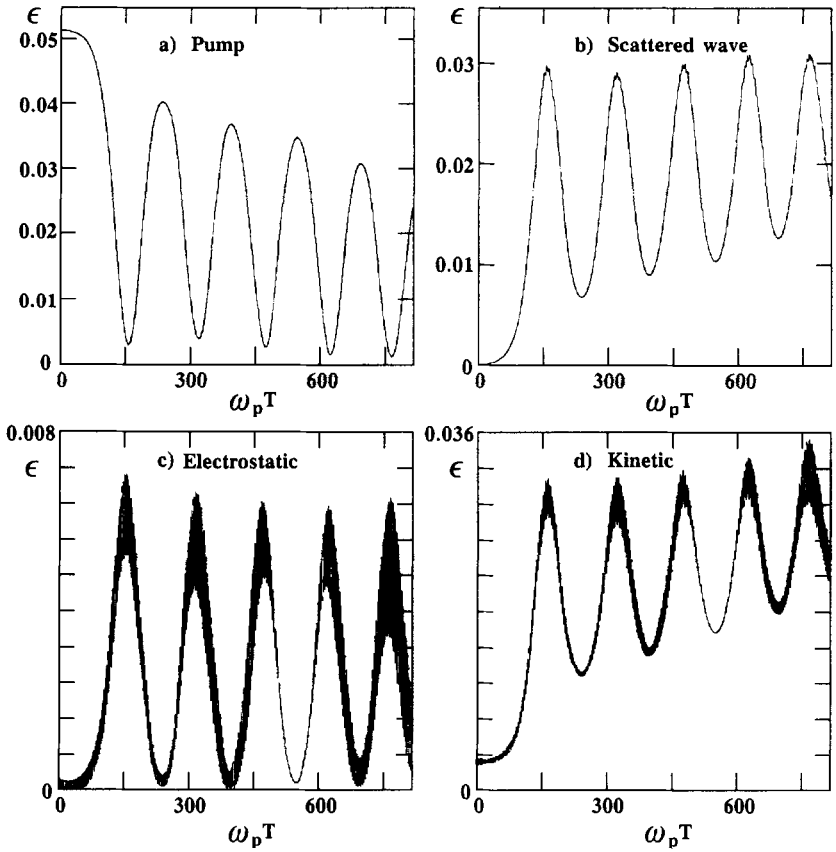

FIG. 3. (a) Time evolution of the energy of the pump for the FRS case. (b) Time evolution of the energy of the scattered wave for the FRS case. (c) Time evolution of the electric energy for the FRS case. (d) Time evolution of the kinetic energy for the FRS case.

i.e., the electromagnetic energy inside the plasma. A Fourier transform of the output data is used to compute the energy for the various mode.

At the first stage of the evolution, Figs. 3b and 3c indeed exhibit an exponential growth related to SRS instability. The theoretical energy growth rate, imputed from linearized fluid equation [6], is

$$\gamma = \frac{\sqrt{2}}{4} \frac{k_e v_{\text{osc}}}{\sqrt{\omega_e \omega_s}} = 0.0405,$$

is found very close to the numerical value obained from a logarithmic plot (0.040).

After the first stage of the instability, the curves of Figs. 3 exhibit an oscillatory behaviour in which energy is transfered back and forth between the pump and the scattered and plasma waves, like a parametric 3-mode coupling. The first saturation

of the electrostatic energy as well as the scattered energy is therefore related to pump depletion at time $\omega_p t = 150$ and can be compared with the Manley–Rowe partition obtained form the envelope equation of the 3-wave coupling process (see, for instance, [6]).

The action conservation between pump and scattered energy is

$$\frac{W_0}{\omega_0} + \frac{W_s}{\omega_s} = \text{const.}$$

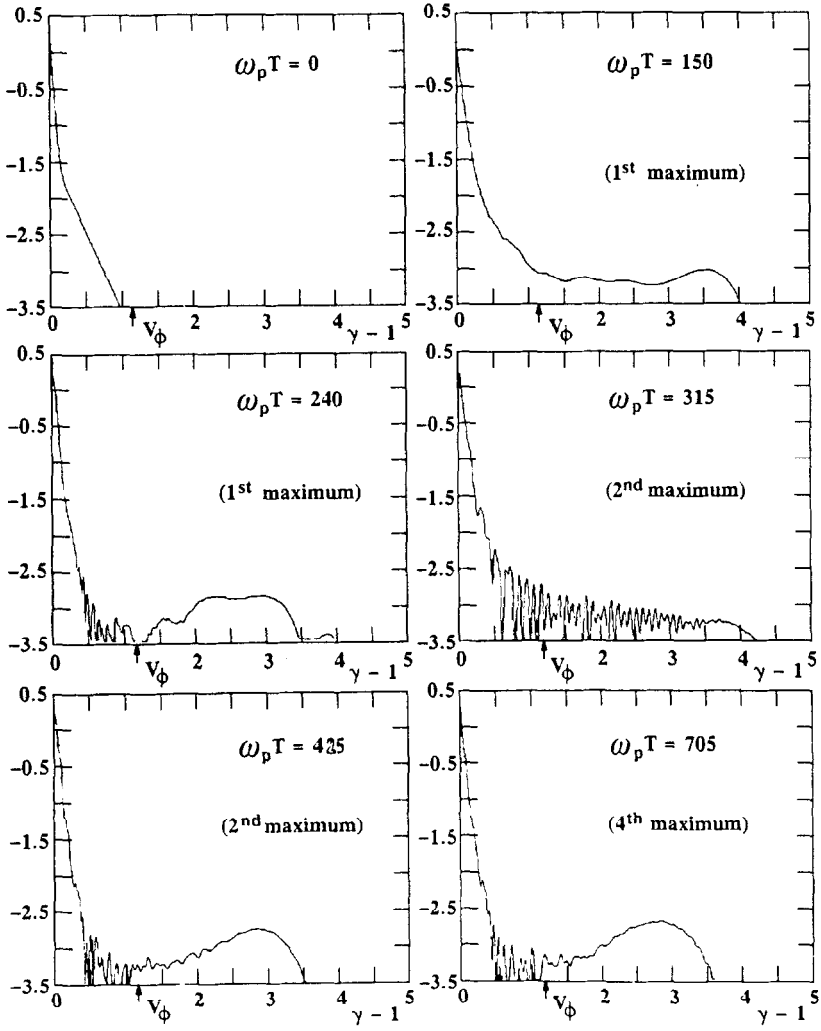

FIG. 4. Plots on a logarithmic scale of the distribution function as a function of energy for the FRS. Notice the small scale oscillations related to the microstructure of the Vlasov equation. The low level of these oscillations is artificially enhanced by the logarithmic scale.

At time $\omega_p t = 0$ (i.e., $W_s = 0$) the intitial action is 0.0197, while at saturation ($\omega_p t = 150$), the correspondng value is 0.0187, assuming complete pump depletion. In the same way, the action for the electrostatic energy at saturation is 0.0216, providing a good agreement between the theoretical prediction of a 3-mode coupling mechanism and the simulation results. In fact, the prediction for SRS with $\omega_0 = 2.6$ and $k_0 = 2.4$ includes two other scattered lights: an upshifted (anti-stokes) radiation (i.e., $\omega_s = \omega_0 + \omega_e$) with a wavenumber 3.45 and a backward scattered light with a wavenumber -0.73. But these wavenumbers lie too far from the accessible multiples of $2\pi/L$ and cannot be excited.

After the first saturation of the electrostatic energy, further behaviour is no longer periodic, and in particular, an important increase of the kinetic energy and a corresponding decrease of the pump energy are to be noticed. These phenomena are connected to the acceleration of particles, as seen in the next paragraph.

3.3. *Distribution Function and Phase Space Representation*

Figure 4 shows the spatially averaged distribution function at $\omega_p t = 0$, then $\omega_p t = 150$ (1st maximum of electric energy), 240 (1st minimum), 315 (2nd maximum), 425 (2nd minimum), and 705 (4th minimum) as a function of the relativistic energy $\gamma - 1$, for particles with positive velocities (in the direction of the incident wave vector). The most important feature is the appearance of a suprathermal population in the range $\gamma - 1 \approx 2 - 4$ (i.e., 1 to 2 MeV). The detailed mechanism of the acceleration can be observed in the $x - p_x$ phase space in Fig. 5.

Figure 5 shows the contour plot in the upperhalf of the phase space ($x - p_x$) plane ($p_x > 0$) together with 3D surface representation of the distribution function in the $x - p_x$ plane, at different time values. Since the accelerated particles correspond to small phase space densities, only contours for $f \leqslant 3\ 10^{-3}$ and 3D representation for $f < 6\ 10^{-3}$ have been drawn. The first Raman oscillation (from $\omega_p t = 0$ to $\omega_p t = 240$) has been represented in Figs. 5a, b, c. The end of the run is shown in Fig. 5d.

These figures exhibit clearly the acceleration of positive velocity particles followed by trapping and formation of vortices around a momentum corresponding to the plasma wave velocity $v_\phi = \omega_e / k_e = 0.88$ or $p_\phi = 1.9$ (corresponding to $\gamma - 1 = 1.14$ in Fig. 4). At the end of each Raman oscillation, a beam is decoupling from the bulk, then a new acceleration occurs. We have estimated the beam density (Fig. 6) and the beam energy as a function of time according to

$$n_{\text{beam}}(t) = \frac{1}{L} \int_0^L \int_{p_\phi}^{p_{\max}} f(x, p_x, t)\, dx\, dp_x$$

FIG. 5. Phase space plots ($f \leqslant 3 \times 10^{-3}$) and the corresponding 3D plots ($f \leqslant 6 \times 10^{-3}$) of the accelerated particles for the FRS. The arrow indicates the momentum p_ϕ corresponding to the phase velocity. The 3D plots are trumcated for f above 6×10^{-3}.

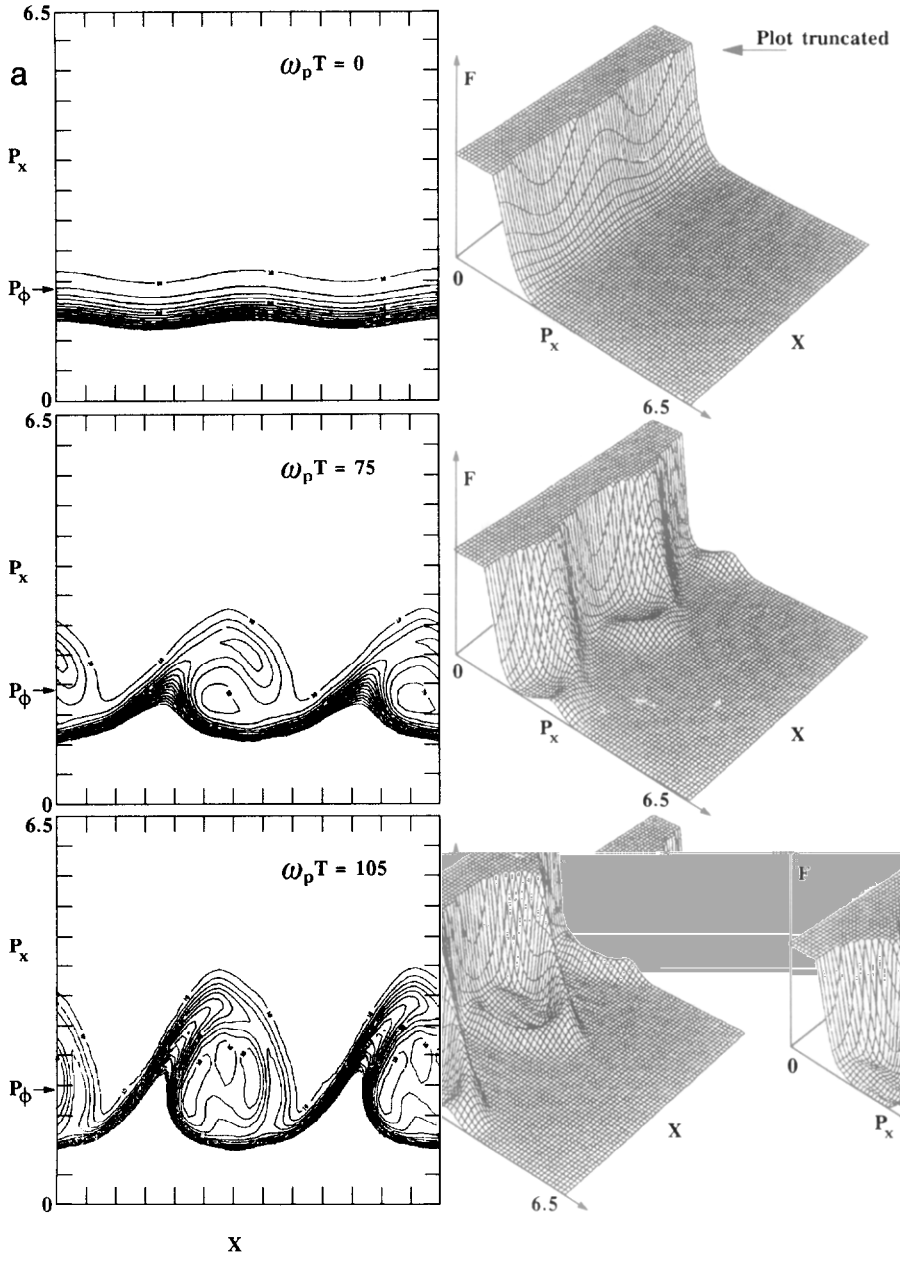
a
$\omega_p T = 0$
$\omega_p T = 75$
$\omega_p T = 105$
P_x
P_ϕ
6.5
0
X
F
Plot truncated

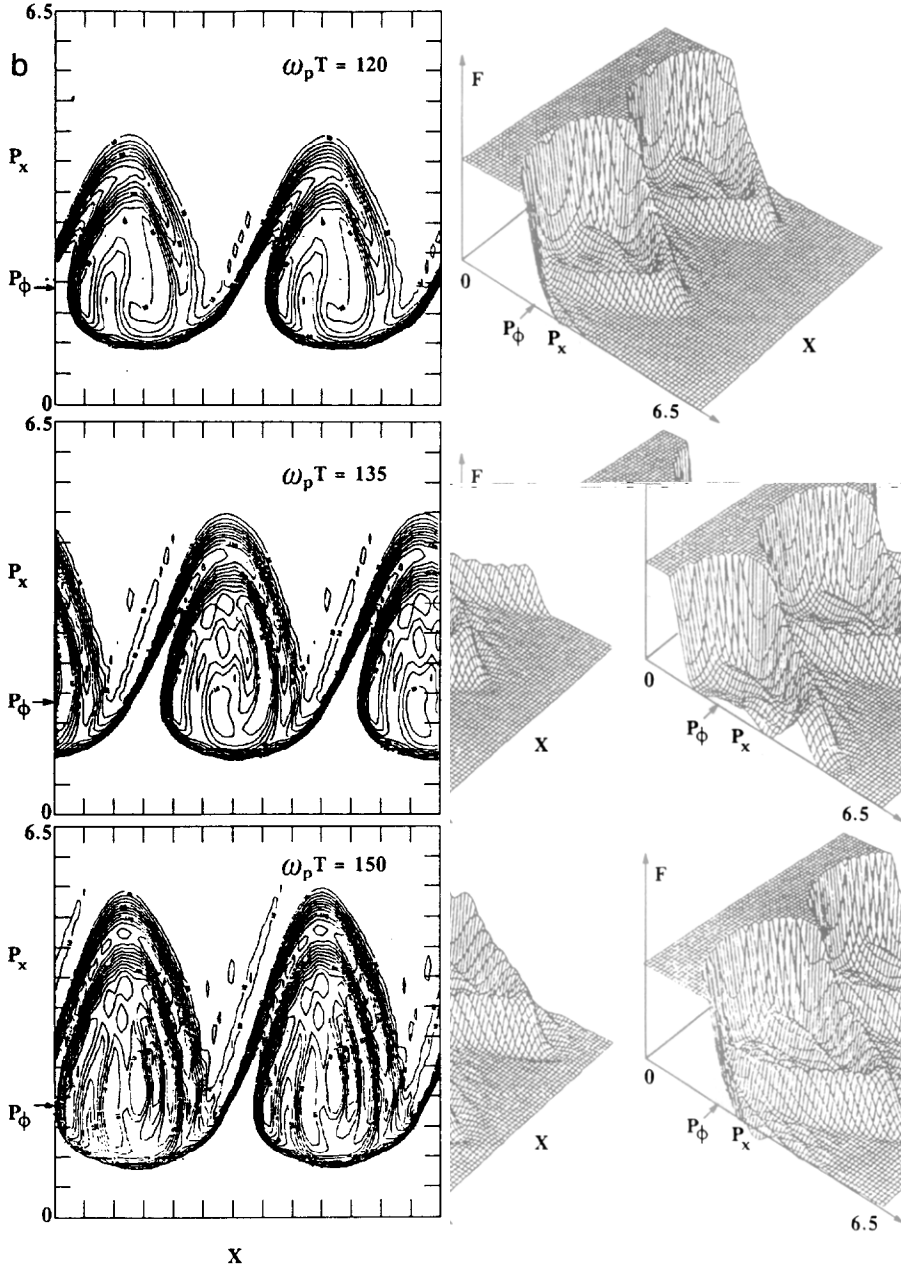

FIG. 5—*Continued*

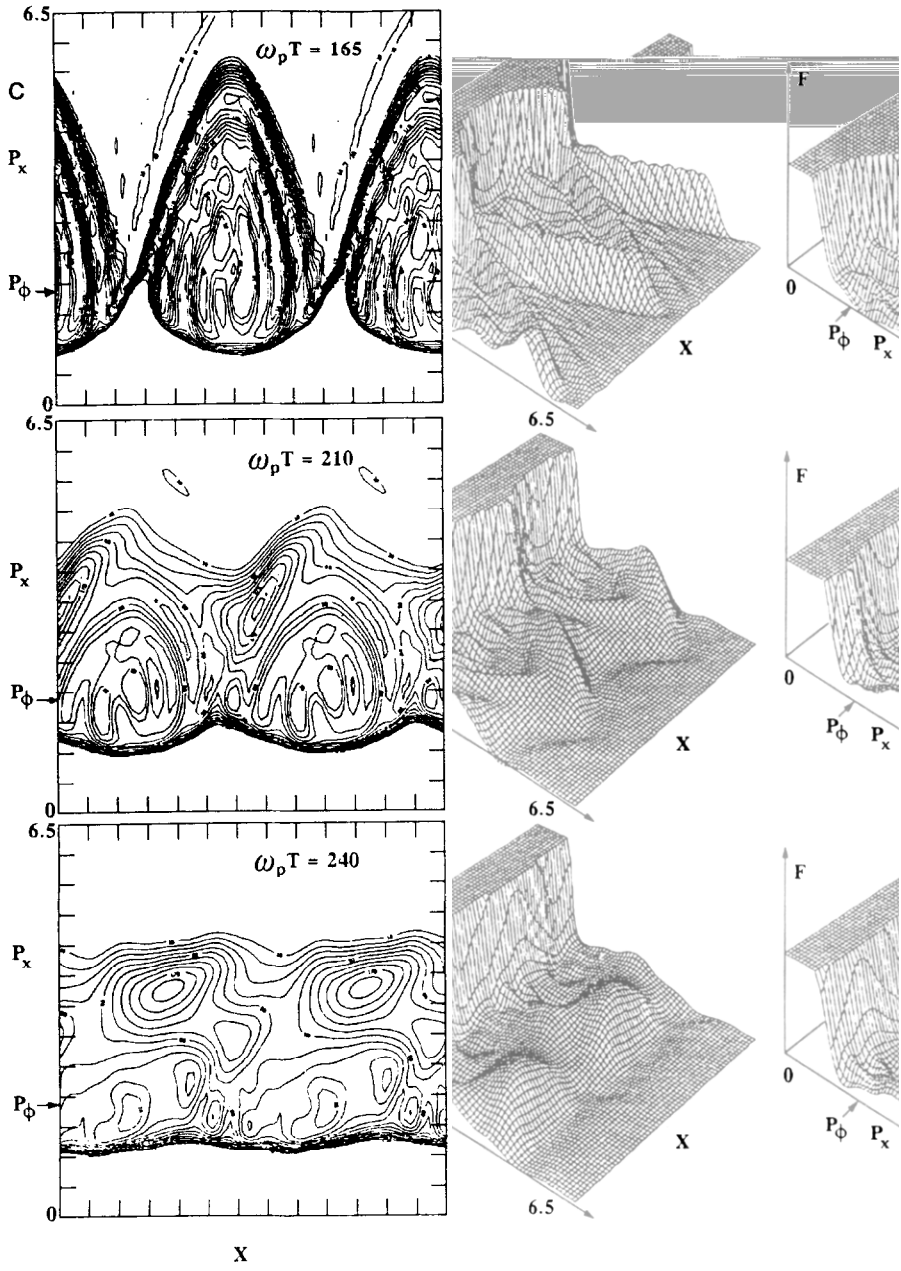

FIG. 5—*Continued*

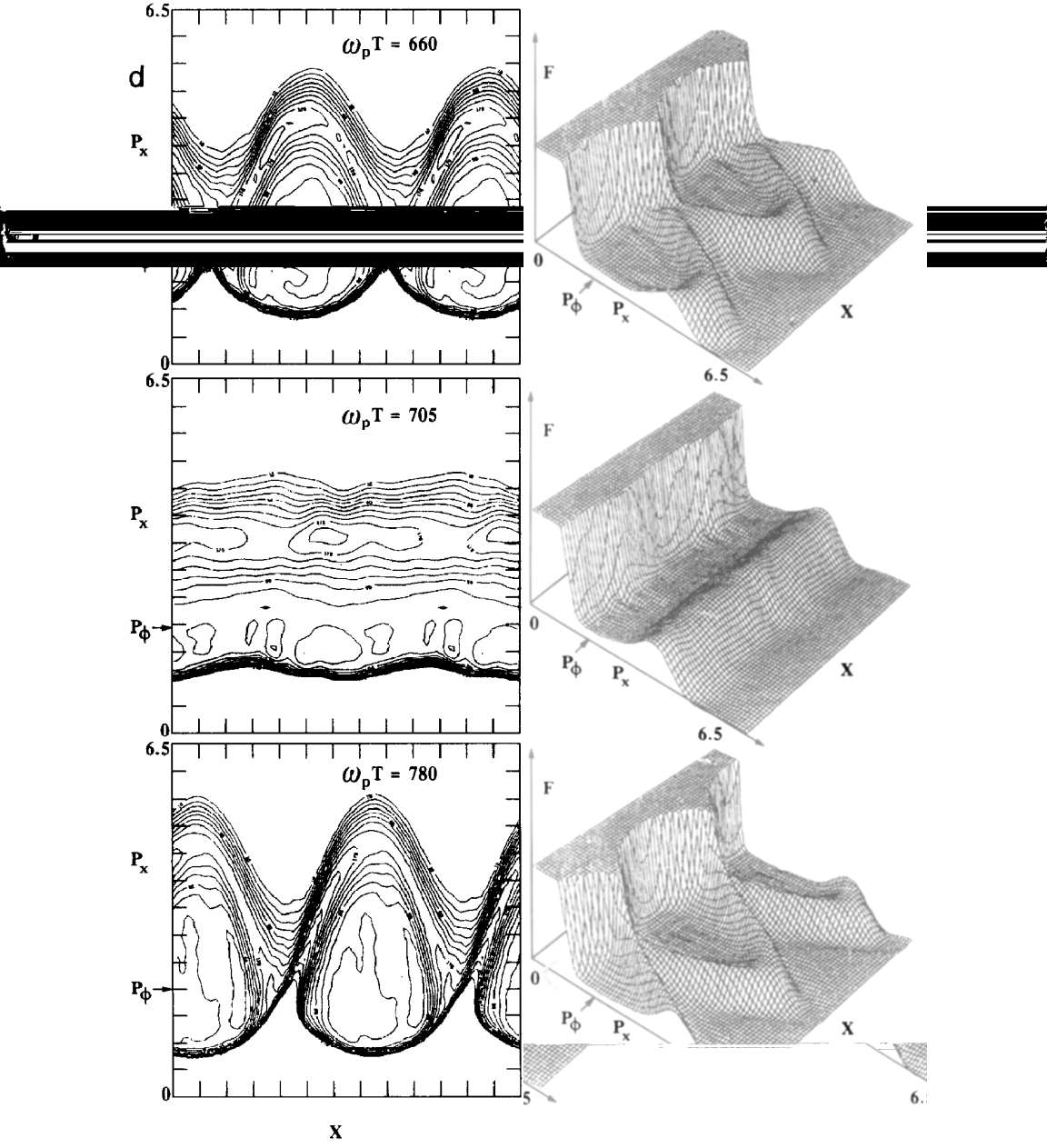

FIG. 5—*Continued*

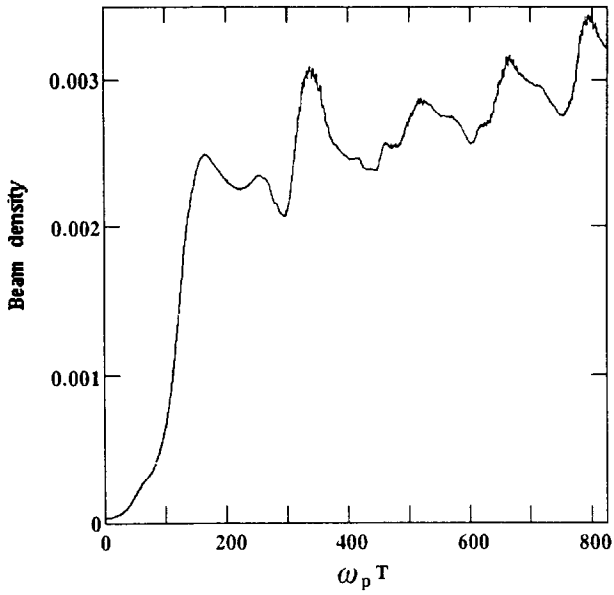

FIG. 6. Time evolution of the high energy beam density for the FRS case.

and

$$\varepsilon_{\text{beam}}(t) = \frac{1}{L}\int_{p_\phi}^{p_{\max}} (\gamma - 1)\, f(x, p_x, t)\, dx\, dp_x.$$

The time behaviour of $\varepsilon_{\text{beam}}$ in nearly the same as n_{beam}. After two periods, these quantities reach a quasi-asymptotic value: The beam has about 0.3% of the total number of electrons but contains about 10% of the total energy.

4. THE BACKWARD RAMAN SCATTERING CASE (BRS)

We now consider the BRS ($\omega_s/k_s < 0$). In that case, the lower phase velocity of the plasma wave involves heavier Landau damping. Thus we require a smaller thermal velocity. A first series of experiments was conducted with a single temperature Maxwellian function with $v_{th} = 0.08c$ ($T = 3.2$ KeV) in a box of length $L = 8.92$ (or $111.5\lambda_d$). The cutoff is now $\pm p_{\max} = \pm 2$. The initial pump wave is

$$k_0 = 3 \times 2\pi/L = 2.113, \qquad \text{corresponding to} = \omega_0 = \sqrt{1 + k_0^2} = 2.338$$

and $E_0 = 0.28$ ($v_{\text{osc}}/c = 0.108$ and $n_0 = 0.18 n_{\text{crit}}$). We select the plasma wave number $k_e = 4 \times 2\pi/L = 2.818$ by slightly perturbing the distribution function. For this

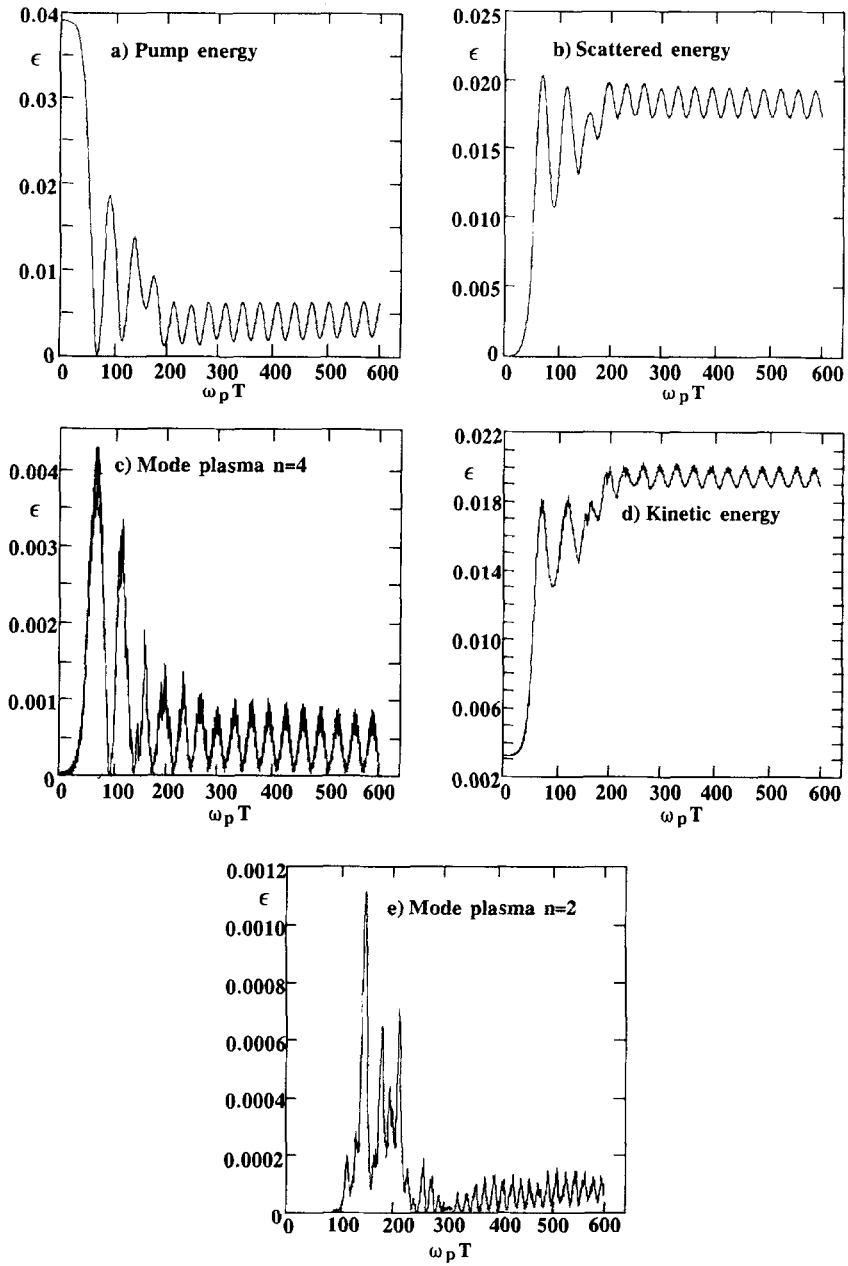

FIG. 7. (a) Time evolution of the pump energy for the BRS case ($v_{th} = 0.08$). (b) Time evolution of the scattered energy for the BRS case ($v_{th} = 0.08$). (c) Time evolution of the energy of the plasma mode with wave vector $k_e = 4 \times 2\pi/L$ for the BRS case ($v_{th} = 0.08$). (d) Time evolution of the kinetic energy of the plasma for the BRS case ($v_{th} = 0.08$). (e) Time evolution of the energy of the plasma mode with $k'_e = 2 \times 2\pi/L = k_e/2$ ($v_{th} = 0.08$).

wavenumber, we have $k_e\lambda_d = 0.22$, so that the Landau damping is negligible. The corresponding frequency is

$$\omega_e = (1 + 3k_e^2 v_{\text{th}}^2)^{1/2} = 1.073.$$

The scattered wave is now

$$k_s = k_0 - k_e = -\frac{2\pi}{L} = -0.705 \qquad \text{(corresponding to } \omega_s = 1.223\text{)}.$$

The mismatch $\Delta\omega = \omega_s - (\omega_0 - \omega_e) = -0.041$ remains small.

In Fig. 7 we present the different modes which are present in the plasma.

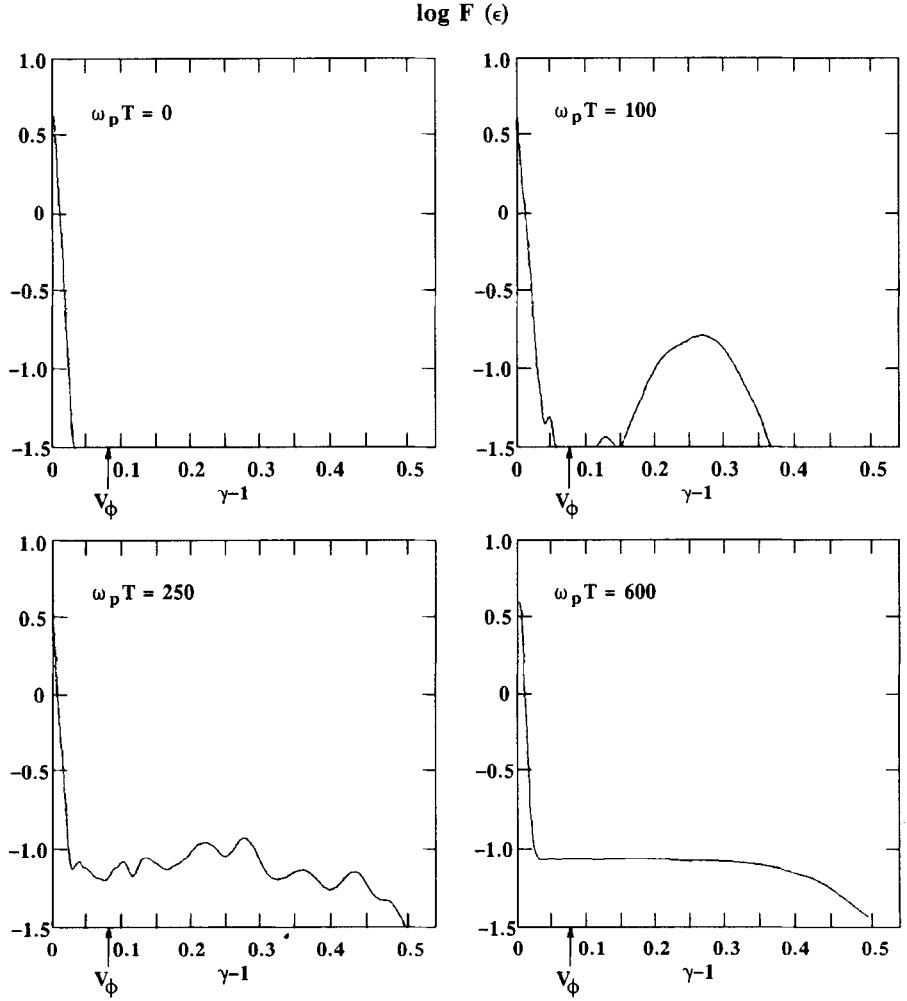

FIG. 8. Plots on a logarithm scale of the distribution function as a function of energy for the BRS ($v_{\text{th}} = 0.08$).

Figures 7a, b, c show the pump energy (k_0), the scattered energy (k_s), and the electrostatic plasma energy (k_e). The kinetic energy is shown in Fig. 7d. In addition, in Fig. 7e we plot the other nonzero mode which developed during the evolution: the electrostatic mode $k'_e = 2 \times 2\pi/L = k_e/2 = 1.409$. For this mode, we note that the matching conditions hold with a scattered forward wavenumber $k'_s = +2\pi/L = +0.705$ ($= -k_s$) and the pump (ω_0, k_0). Indeed, we have

$$\omega_0 - \omega'_e = 1.319 \quad \text{as compared with} \quad \omega'_s = 1.223 \qquad \text{(mismatch 0.096)}.$$

For these intitial conditions, BRS as well as FRS are present. In fact, we have conidered only an initial excitation of BRS instability. Even if FRS has not been initialy excited, it has grown but with a relatively low level (see Figs 7c and 7e). In that case, BRS remains the dominant phenomena.

During the first stage of BRS (i.e., between $\omega_p t = 0$ and $\omega_p t = 65$, corresponding to the first pump depletion and the corresponding scattered or electrostatic energy saturation) the Manley–Rowe partition can be verified:

- between the pump and scattered energy, the action is 0.01677 at $\omega_p t = 0$ and 0.01659 at $T = 65$;

- between the pump and electrostatic energy: the action is 0.01677 at $\omega_p t = 0$ and 0.01674 at $\omega_p t = 65$.

Figure 8 shows the spatially averaged distribution function as a function of $\gamma - 1$ for $\omega_p t = 0$, 100, 250, and 600. The phase velocity is smaller than the FRS case. I.e., $v_\phi = 0.38$ ($= 4.75\ V_{\text{th}}$) corresponding to $p_\phi = 0.41$ or $\gamma - 1 = 0.081$. Contrary to FRS, the distribution function exhibits a quasi-plateau extending to $\gamma - 1 \approx 0.4$.

The formation of this structure can be viewed in the $x - p_x$ plots (Fig. 9): since we have excitated the mode $k_e = 4 \times 2\pi/L$, we forecast the appearance of a four-vortex structure. But the presence of mode $k_e/2$ generated by FRS will produce a fusion of the four-vortex into a two-vortex structure, followed by a cleaning of the microstructure, to end up with a quasi homogeneous plateau at $\omega_p t = 600$.

A second series of experiments is conducted by increasing v_{th} up to 0.11 (the other parameter being unchanged excepting the cutoffs $\pm p_{\max} = \pm 3$) corresponding to $k_e \lambda_D = 0.31$. For this value, it may be conjectured that the Landau damping is now strong enough to significantly reduce the level of the electrostatic mode k_e with respect to the FRS mode $k'_e = k_e/2$, after a certain time. In Fig. 10, we plot the phase space contours at time $\omega_p t = 300$, 340, and 400 showing indeed the

FIG. 9. Phase space plots and the corresponding 3D plots for the BRS ($v_{\text{th}} = 0.08$). Although the simulation is performed with $p_{\max} = 2$, the upper half of the phase space plane is represented up to $p = 1.25$. The arrow indicates the momentum corresponding to the phase velocity. The 3D plots are truncated.

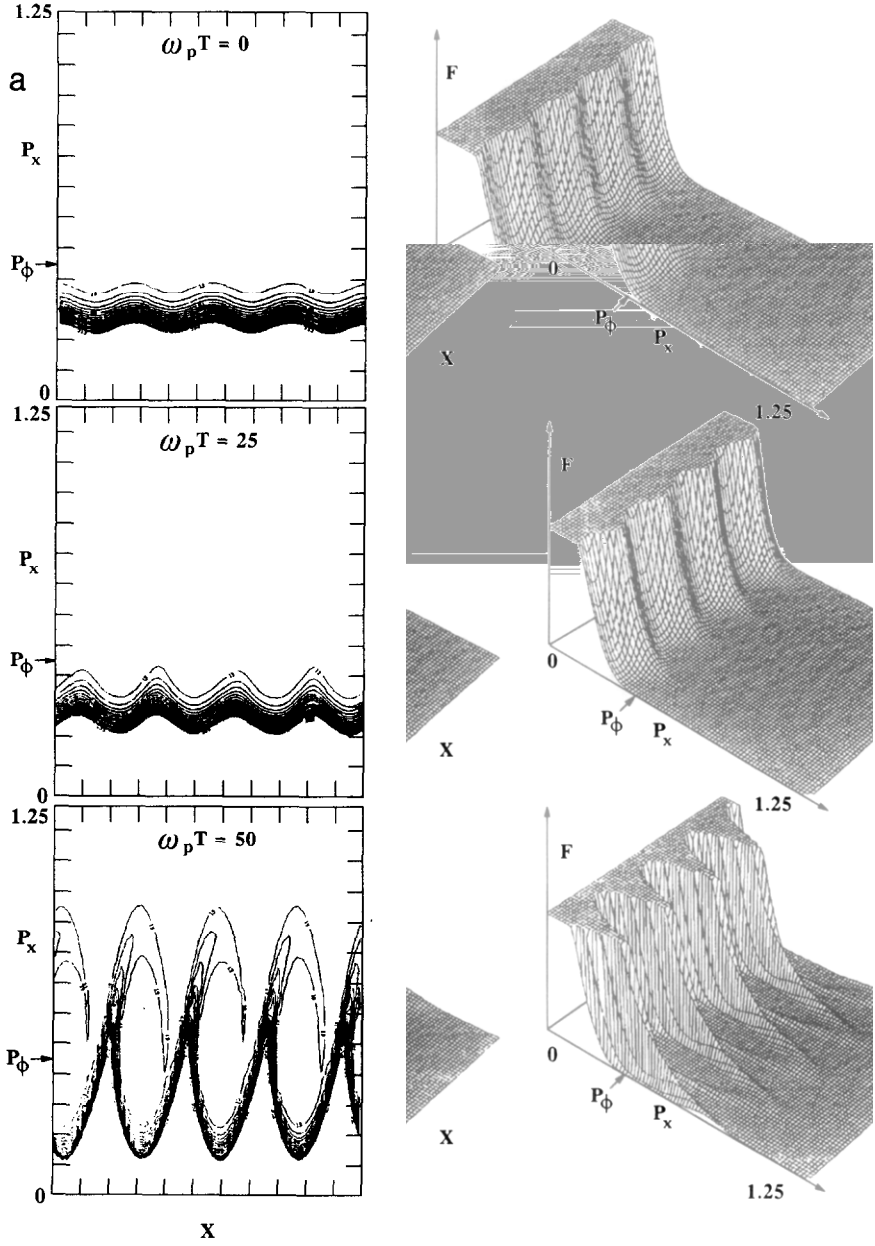
a
1.25
$\omega_p T = 0$
P_x
P_ϕ
0
1.25
$\omega_p T = 25$
P_x
P_ϕ
0
1.25
$\omega_p T = 50$
P_x
P_ϕ
0
X
F
0
P_ϕ
P_x
X
1.25
F
0
P_ϕ
P_x
X
1.25
F
0
P_ϕ
P_x
X
1.25

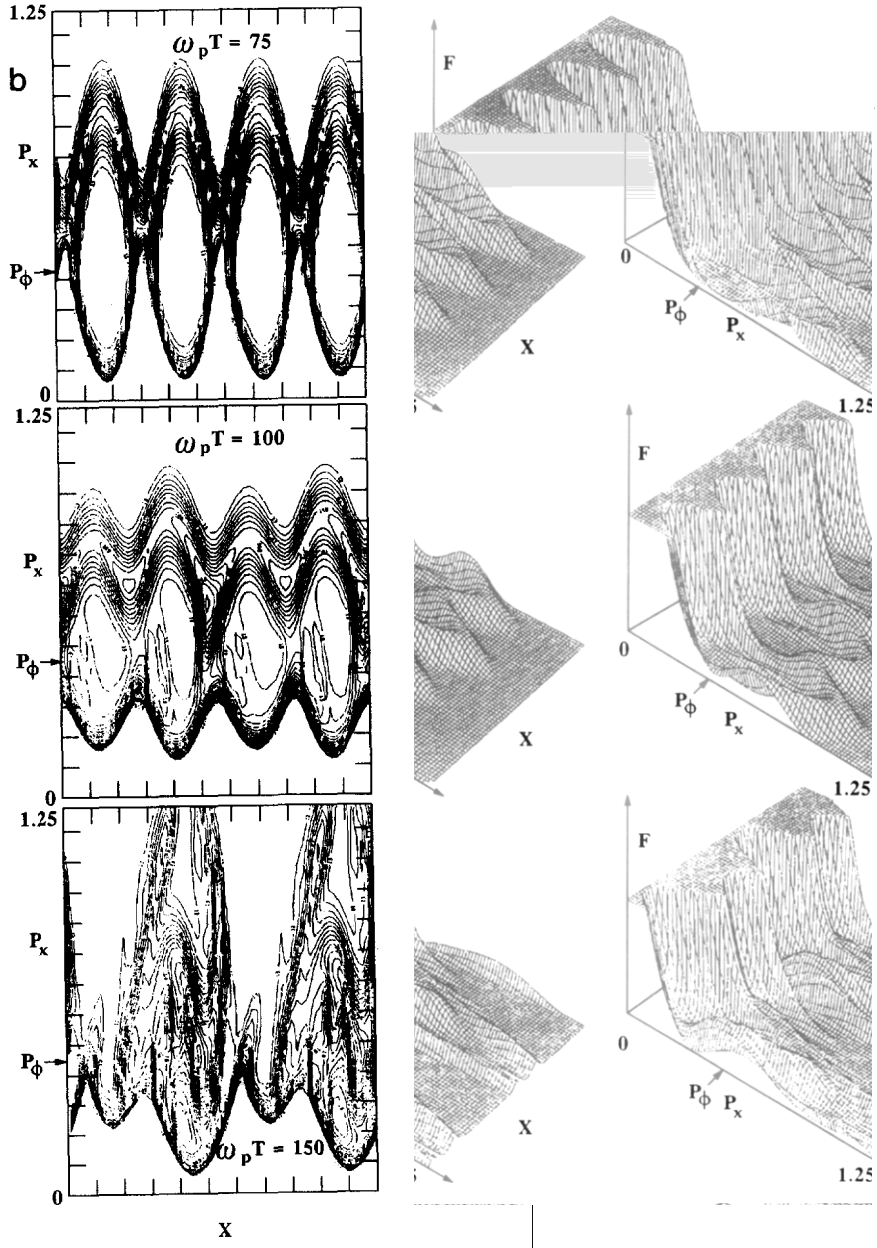

FIG. 9—*Continued*

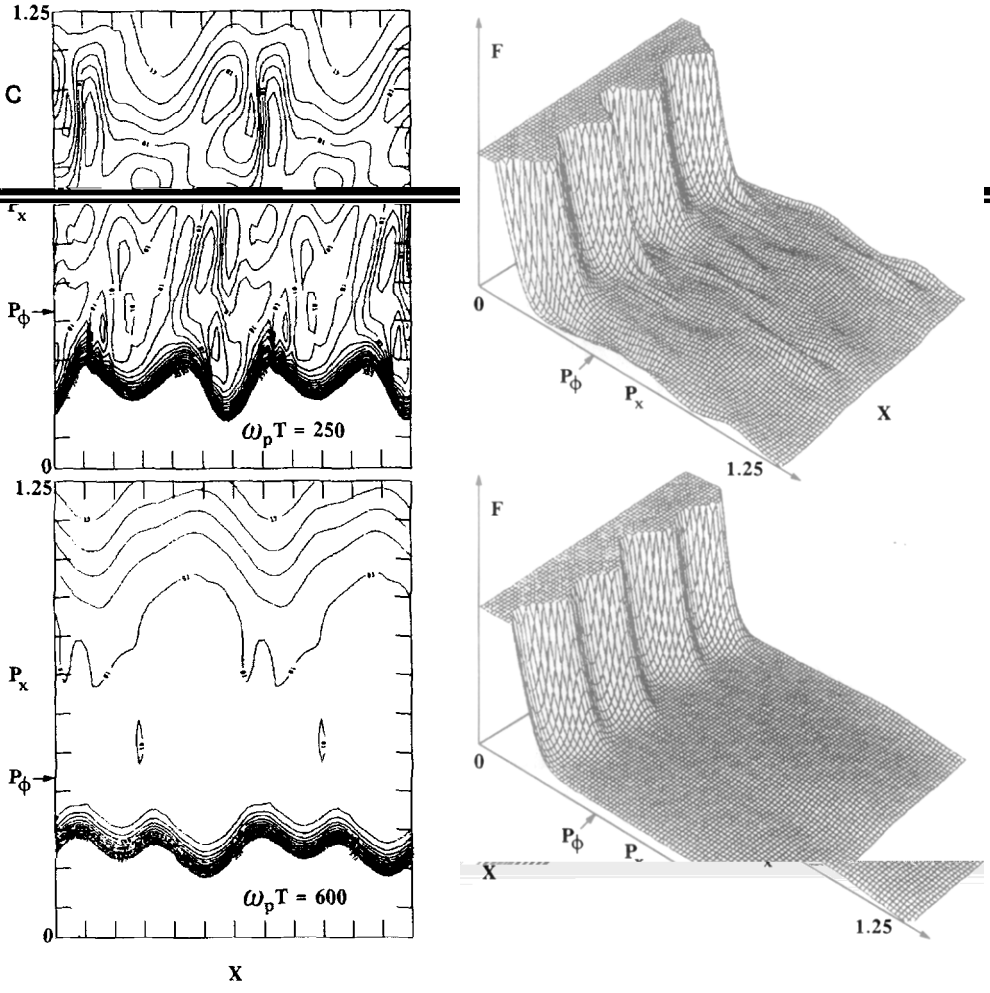

FIG. 9—*Continued*

appearance of acceleration of particles due to FRS followed by trapping. Figure 10d shows the 3D plot of the function at $\omega_p t = 400$. Summarizing the time history of SRS:

— first the system starts with backward SRS instability, leading to the 1st electron plateau ($\gamma - 1 \approx 0.4$);

— then we have forward SRS appearing later, giving very energetic particles with $\gamma - 1 \approx 1.5$.

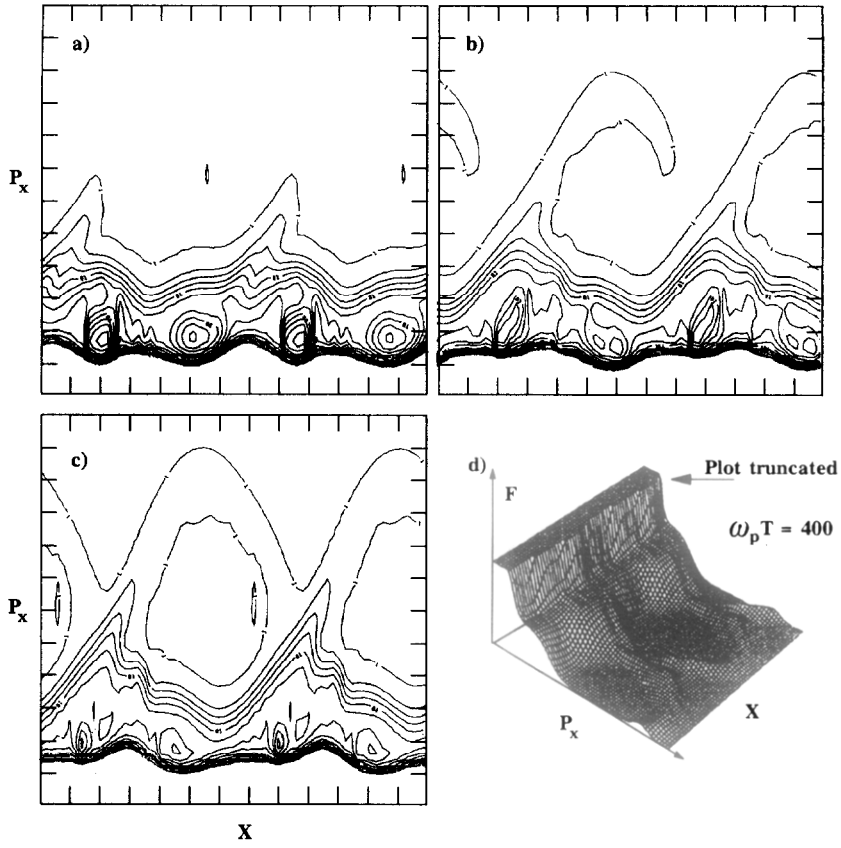

FIG. 10. Phase space plots for the BRS at higher thermal velocity ($v_{th} = 0.11$): (a) $\omega_p t = 300$; (b) $\omega_p t = 340$; (c) $\omega_p t = 400$, (d) corresponding 3D plot for $\omega_p t = 400$.

5. DISCUSSION

The Vlasov code provides an excellent resolution all over the phase space, including very low density regions. In the present problem, in which electrons are accelerated at high momenta, a small fraction of the particles (which cannot be estimated in advance) are distributed over a large region of phase space. Without using a prohibitive number of particles, a PIC code will only have a few particles to scatter about in these very low density regions. The Vlasov code provides a good resolution naturally, allowing a relatively economical calculation of these phase space low density structures, which are simply invisible in particle codes.

Detailed comparison with particle orbit theories or Manley–Rowe relations are now under consideration and will be presented in a forthcoming paper. Although

we have restricted ourselves to FRS and BRS in a small periodic plasma, we have also applied the Eulerian Vlasov code to other cases of interest, such as beat wave acceleration (with two initial pumps ω_0, k_0 and ω_1, k_1) or the inclusion of ion motion to take Brillouin scattering into account.

The code has recently also been extended to the bounded case without any difficulties. Bounded plasma models are closer to real plasma than periodic models. Since a longer system must be considered (about 80–100 beat wavelengths) the number N_x has to be substantially increased, but the available vector supercomputers are now able to deal with such codes.

Finally, we have considered here a simplified macroscopic description for the perpendicular motion of the particles, assuming that the mean velocity $u_x \ll c$. Whether a microscopic description would significantly alter the dynamics especially for the strongly accelerated particles is still an open question. The answer could be given by extending our 1D Vlasov model to a full $1\frac{1}{2}$D one. I.e., considering a distribution function $f(x, p_x, p_y)$, the basic numerical steps as described by (3)–(4) are unchanged. The problem is only in memory size and CPU time. But again it is still within the capacity of the available supercomputers.

Appendix

To show how the numerical scheme presented in Section 2.2 integrates the Vlasov equation (11), consider first what happens to the distribution function as the operator $(\hat{H}/2)\,\hat{P}_x\hat{H}/2$ is applied to the initial distribution function $f_n(x, p_x, t = n\,\Delta T)$; $\hat{H}/2$ and $\hat{p}_x$ denoting respectively the shift in position and in momentum. Thus we obtain

$$f(x, p_x, t_{n+1}) = f(\bar{x}, \bar{p}_x, t_n)$$

with

$$\bar{x} = x - \frac{p_x}{m\gamma}\,\Delta T - e(E_x^* + u_y^* B_z^*)\,\frac{\Delta T^2}{2m\gamma^3} + O(\Delta T^3) \tag{20}$$

and

$$\bar{p}_x = p_x + e(E_x^* + u_y^* B_z^*)\,\Delta T + O(\Delta T^3), \tag{21}$$

where

$$E_x^* = E_x\left(x - \frac{p_x}{m\gamma}\,\frac{\Delta T}{2}\right)$$

$$B_z^* = B_z\left(x - \frac{p_x}{m\gamma}\,\frac{\Delta T}{2}\right).$$

By using the relation (12) we have

$$u_y^* = \frac{1}{2}(u_y^n + u_y^{n+1}) = u_y^{n+1} + \frac{e}{2m} E_y^{n+1/2} \Delta T \tag{22}$$

and, therefore,

$$\bar{x} = x - \frac{p_x \Delta T}{m\gamma} - \frac{e}{m\gamma^3}(E_x^* + u_y^{n+1} B_z^*) \frac{\Delta T^2}{2} + O(\Delta T^3) \tag{23}$$

and

$$\bar{p}_x = p_x + e(E_x^* + u_y^{n+1} B_z^*) \Delta T + \frac{e^2}{2m} E_y^* B_z^* \Delta T^2 + O(\Delta T^3). \tag{24}$$

On the other hand, let us consider the equations describing one-dimensional particle motion,

$$\frac{dx}{dt} = v_x \tag{25}$$

$$\frac{d}{dt}\left[\frac{mv_x}{(1 - v_x^2/c^2)^{1/2}}\right] = -e(E_x + u_y B_z) \tag{26}$$

and, again, Eq. (12).

From (25) we can write

$$x^n = x^{n+1} - v_x^{n+1/2} \Delta T = x^{n+1} - v_x^{n+1} \frac{\Delta T}{2} - v_x^n \frac{\Delta T}{2}. \tag{27}$$

From (26) and since

$$\frac{d}{dt}\left(\frac{mv_x}{\sqrt{1 - v_x^2/c^2}}\right) = m \frac{dv_x}{dt}\left(1 - \frac{v_x^2}{c^2}\right)^{-3/2} \tag{28}$$

we have

$$v_x^n = v_x^{n+1} + \frac{e}{m} \Delta T (E_x^{n+1/2} + u_y^{n+1/2} B_z^{n+1/2}) \left[1 - \left(\frac{v_x^n + v_x^{n+1}}{2c}\right)^2\right]^{+3/2} \tag{29}$$

which leads to

$$x^n = x^{n+1} - \frac{p_x^{n+1} \Delta T}{m\gamma} - \frac{e}{m\gamma^3}(E_x^{n+1/2} + u_y^{n+1/2} B_z^{n+1/2}) \frac{\Delta T^2}{2}, \tag{30}$$

where we have replaced v_x by $p_x/m\gamma$.

A similar analysis for the momentum variable p_x leads to

$$p_x^n = p_x^{n+1} + e(E_x^{n+1/2} + u_y^{n+1} B_z^{n+1/2})\,\Delta T + \frac{e^2}{2m} E_y^{n+1/2} B_z^{n+1/2}\,\Delta T^2 + O(\Delta T^3). \tag{31}$$

By comparing Eqs. (20), (21) and (30), (31), we see without difficulty that the splitting scheme integrates the distribution function along the characteristics correctly to second order in ΔT.

ACKNOWLEDGMENTS

The authors are indebted to the Centre de Calcul Vectoriel pour la Recherche (École Polytechnique, Palaiseau, France) for computer time allocation on the CRAY-2 computer, and to CRAY-Canada for computer time allocation on the CRAY-1-S at Dorval (Québec). P. Bertrand and A. Ghizzo acknowledge the hospitality of the Tokamak de Varennes (Canada) and the partial financial support of France-Québec during part of this work.

REFERENCES

1. T. TAJIMA AND J. M. DAWSON, *Phys. Rev. Lett.* **43**, 267 (1979).
2. T. KATSOULEAS AND J. M. DAWSON, *Phys. Rev. Lett.* **51**, 392 (1983).
3. C. JOSHI, T. TAJIMA, AND J. M. DAWSON, *Phys. Rev. Lett.* **47**, 1287 (1981).
4. H. FIGUEROA, C. JOSHI, H. AZECHI, N. A. EBRAHIM, AND K. ESTABROOK, *Phys. Fluids* **27**, 1887 (1984).
5. S. AITHAL, P. LAVIGNE, M. PÉPIN, T. W. JOHNSTON, AND K. ESTABROOK, *Phys. Fluids* **30**, No. 12, 3832 (1987).
6. D. W. FORSLUND, J. M. KINDEL, E. L. LINDMAN, *Phys. Fluids* **18**, 1002, 1017 (1975).
7. K. ESTABROOK, W. L. KRUER, AND B. F. LASINSKI, *Phys. Rev. Lett.* **45**, 1399 (1988).
8. F. HIOB AND A. J. BARNARD, *Phys. Fluids* **26**, 10 (1983).
9. A. GHIZZO, B. IZRAR, P. BERTRAND, E. FIJALKOW, M. R. FEIX, AND M. SHOUCRI, *Phys. Lett. A* **120**, 191 (1987).
10. A. GHIZZO, B. IZRAR, P. BERTRAND, E. FIJALKOW, M. R. FEIX, AND M. SHOUCRI, *Phys. Fluids* **31**, 72 (1988).
11. G. KNORR AND C. G. CHENG, *J. Comput. Phys.* **22**, 330 (1976).
12. R. J. GAGNÉ AND M. M. SHOUCRI, *J. Comput. Phys.* **24**, 445 (1977).
13. M. M. SHOUCRI AND R. J. GAGNÉ, *J. Comput. Phys.* **27**, 315 (1978).
14. J. P. BORIS AND D. L. BOOK, *Methods Comput. Phys.* **16**, 85 (1976).
15. A. GHIZZO, Ph.D. thesis, University of Nancy, France, 1987 (unpublished).
16. [illegible] (1975).
17. F. DRAKE, P. K. KAW, Y. C. LEE, G. SCHMIDT, C. S. LIU, AND M. N. ROSENBLUTH, *Phys. Fluids* **17**, 778 (1974).